First-principles investigation of Sr-Ce-M-O perovskites for solar thermochemical water splitting

Sachin Kumar[1], Pritam Ghosh[1], and Gopalakrishnan Sai Gautam[1,*]

[1]Department of Materials Engineering, Indian Institute of Science, Bengaluru, 560012, India

[*]Email: saigautamg@iisc.ac.in

September 3, 2025

Abstract

Using density functional theory based calculations, we systematically examine the utility of Sr-M-O and Sr-Ce-M-O perovskites for solar thermochemical water splitting, a promising route for sustainable hydrogen production. Importantly, we identify $Sr_{0.5}Ce_{0.5}MnO_3$ and $Sr_{0.5}Ce_{0.5}CrO_3$ to be promising candidates, exhibiting optimal oxygen vacancy formation energy and 0 K thermodynamic stability.

1 Introduction

The escalating global energy demand and the pressing need to mitigate climate change necessitate a transition towards sustainable and carbon-neutral energy carriers. [1, 2] Hydrogen, with its high energy density and zero-emission combustion, stands out as a promising alternative to fossil fuels. [3,4] To produce green hydrogen on a large scale, solar thermochemical water splitting (STWS) cycles offer a direct and efficient pathway by harnessing concentrated solar energy to drive the endothermic dissociation of water, typically via a two-step redox cycle involving a metal oxide (see Section I of the electronic supplementary information−ESI). [5,6]

The STWS cycle generally comprises:

1. **Thermal Reduction (TR):** $MO_x \rightarrow MO_{x-\delta} + \delta/2\ O_2(g)$ [at T >1673 K]
2. **Water Splitting (WS):** $MO_{x-\delta} + \delta\ H_2O(g) \rightarrow MO_x + \delta\ H_2(g)$ [at T between 873-1473 K]

Non-stoichiometric cerium dioxide (CeO_2) is the current state-of-the-art material for STWS owing to its rapid redox kinetics and structural stability. [7,8] However, CeO_2 requires very high reduction temperatures (¿ 1500 °C) to achieve even modest extent of reduction (i.e., δ), limiting practical solar-to-hydrogen efficiency. [9] Specifically, CeO_2 exhibits an enthalpy of reduction (ΔH_{red})∼4 eV per oxygen vacancy, which is significantly higher than the ideal range of 3.4-3.9 eV/vacancy for optimal STWS operating conditions. [10] Offering tunable redox properties, perovskite oxides (ABO_3) have emerged as attractive alternatives to CeO_2 for STWS, exhibiting favourable thermodynamics for reduction at moderate temperatures (between

1200–1400 °C) and good kinetic performance. [11–13] Most perovskites, however, exhibit redox activity primarily on the B-site transition-metal cation, restricting the configurational entropy change upon reduction (ΔS_{red}) relative to ceria, [14] eventually limiting amount of H_2 generated.

At any T, the Gibbs energy of reduction ($\Delta G_{\mathrm{red}} = \Delta H_{\mathrm{red}} - T\Delta S_{\mathrm{red}}$) governs the extent of reduction. For a given ΔH_{red}, a higher ΔS_{red} permits greater reduction extent at a given temperature, or, equivalently, greater reduction at lower temperatures. Consequently, designing perovskites with enhanced ΔS_{red} by enabling multi-site redox is a key strategy for improving STWS performance. Previous work on $Ca_{0.5}Ce_{0.5}MnO_3$ demonstrated the feasibility of simultaneous A-site (Ce) and B-site (Mn) redox, leading to improved STWS characteristics. [15, 16] Building upon this concept, Sr-based perovskites are of particular interest owing to Sr's larger ionic radius, which may accommodate redox-active Ce more readily [17, 18] and also influence oxygen mobility. Nevertheless, a systematic investigation of Sr-based quaternary perovskites incorporating Ce for STWS is currently lacking.

Our study employs density functional theory (DFT) based calculations to systematically explore the potential of Sr-M-O ternary ($SrMO_3$) and Sr-Ce-M-O quaternary ($Sr_{0.5}Ce_{0.5}MO_3$) perovskites (where M = Ti, V, Cr, Mn, Fe, or Co) as potential STWS materials. We exclude Sc and Zn from the $3d$ series since they are not redox-active, while we exclude Cu since it typically does not acquire a +3 oxidation state and form perovskite structures. [19] We also exclude Ni since we could not obtain a reliable experimental $SrNiO_3$ structure, which can be attributed to its instability under ambient pressures. [20] We focus on elucidating the oxygen vacancy formation energy ($E[V_O]$), a proxy for ΔH_{red}, and 0 K thermodynamic stability to identify candidates potentially capable of simultaneous A-site (Ce^{4+}) and B-site (M-cation) reduction. Such dual-site redox activity can achieve higher ΔS_{red}, [21] potentially surpassing CeO_2 in STWS efficiency. Our findings identify $Sr_{0.5}Ce_{0.5}CrO_3$ and $Sr_{0.5}Ce_{0.5}MnO_3$ systems to be promising candidates, exhibiting optimal $E[V_O]$ and thermodynamic stability, paving the way for a new class of high-performance STWS materials.

2 Methods

All spin-polarized DFT calculations were performed using the Vienna ab initio simulation package (VASP). [22, 23] We employed the projector augmented-wave potentials, [24] and described the exchange-correlation interactions using the strongly constrained and appropriately normed (SCAN) functional. [25] A Hubbard U correction (i.e., SCAN+U) was applied to the $3d$ orbitals of M and the $4f$ orbitals of Ce to accurately describe the strongly correlated electrons, with the U values taken from literature. [26–28]We used a plane-wave energy cutoff of 520 eV and sampled the irreducible Brillouin zone using Γ-centered Monkhorst-Pack [29] k-point meshes with a density of at least 48 $Å^{-1}$. We relaxed all structures, i.e., allowed cell shape, volume, and ionic positions to change without preserving symmetry, until atomic forces were below —0.01— eV/Å and the total energy converged to 10^{-5} eV.

Initial structures for ternary $SrMO_3$ perovskites were obtained from the inorganic crystal structure database (ICSD). [30] For each $SrMO_3$ system, we considered various known polymorphs, as available in the ICSD, to identify the ground state structure (see Table S1 of the ESI). Quaternary $Sr_{0.5}Ce_{0.5}MO_3$ structures were generated by substituting 50% of Sr atoms with Ce in the A-site of the ground state, ternary $SrMO_3$ supercells. We utilized the pymatgen library [31] to generate symmetrically distinct A-site cation orderings (i.e., Sr and Ce configurations) within each $SrMO_3$ unit cell or supercell.

The thermodynamic stability of pristine perovskites was evaluated by calculating the energy above the convex hull (E_{hull}) with respect to other competing phases. For calculating E_{hull}, we considered all ordered unary, binary, ternary, and quaternary Sr-Ce-M-O compounds, as available in the ICSD, excluding intermetallics, as compiled in Section V of the ESI. While E_{hull} ¿ 0 indicates instability (or metastability) at 0 K, entropic contributions at high operational temperatures can stabilize some metastable phases to an extent. [15] Convex hull plots of ternary and quaternary systems are compiled in Figures S1 and S2 of the ESI.

We calculated neutral $E[V_O]$ within supercells of the pristine ground-state $SrMO_3$ and $Sr_{0.5}Ce_{0.5}MO_3$ structures. We maintained a minimum distance of 8 Å between periodic vacancy images to reduce spurious interactions between the vacancy defect and its periodic images. [15] Specifically, we used 3×3×3 supercells for cubic and tetragonal systems, 2×2×2 supercells for orthorhombic and monoclinic systems and 2×2×1 supercells for hexagonal systems, respectively, to ensure convergence of $E[V_O]$ to within ±0.1 eV. [32] We used the following equation to calculate $E[V_O]$:

$$E[V_O] = E^{\mathrm{SCAN+U}}_{\mathrm{defective}} - E^{\mathrm{SCAN+U}}_{\mathrm{pristine}} + \frac{1}{2}E^{\mathrm{SCAN}}_{\mathrm{O_2(g)}} \tag{1}$$

where $E^{\mathrm{SCAN}+U}_{\mathrm{defective}}$ and $E^{\mathrm{SCAN}+U}_{\mathrm{pristine}}$ represent the total energy of the supercell with one oxygen vacancy and the pristine supercell, respectively, calculated with SCAN+U. $E^{\mathrm{SCAN}}_{\mathrm{O_2(g)}}$ is the total energy of an isolated oxygen molecule in its triplet ground state, calculated using the SCAN functional. We considered all symmetrically distinct oxygen sites for the formation of the vacancy. For defective structures, we relaxed the ionic positions only with fixed lattice parameters (from the corresponding relaxed pristine ground state structure). We prioritized the lowest $E[V_O]$ among different vacancy sites for identifying candidate compositions.

3 Results and Discussion

3.1 Ternary perovskites

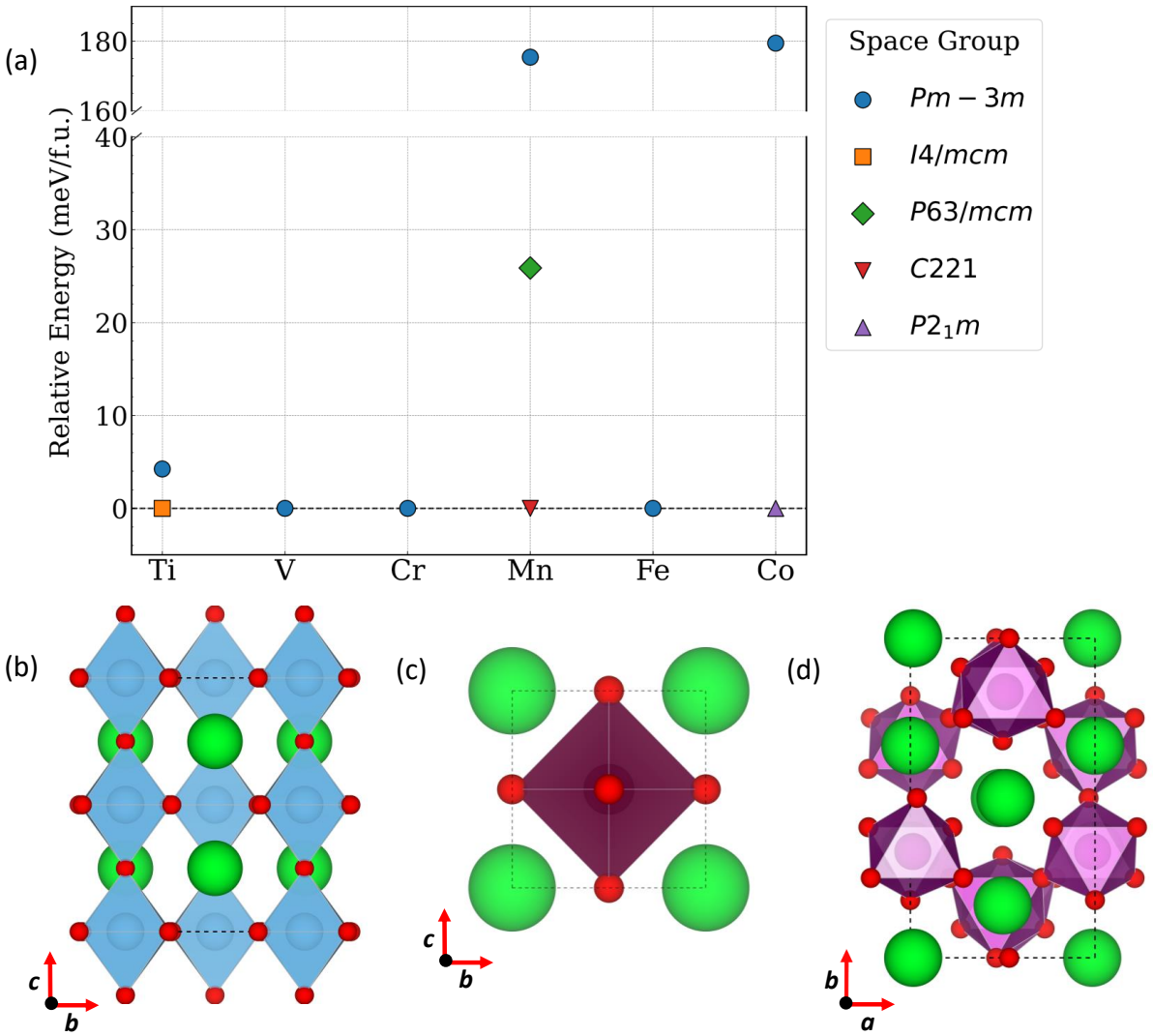

Figure 1: (a) Energy relative to the calculated ground state for different $SrMO_3$ polymorphs considered. (b-d) Ground state polymorphs of $SrMO_3$ ternary perovskites, namely (b) $SrTiO_3$, (c) $SrVO_3$, $SrCrO_3$, $SrFeO_3$, and $SrCoO_3$, and (d) $SrMnO_3$. Green and red spheres are Sr and O, respectively, while colored polyhedra represent MO_6 octahedra.

First, we use DFT to identify the ground state structures of ternary $SrMO_3$ perovskites, among the various polymorphs reported in the ICSD, with Figure 1a plotting the energies (in meV/f.u.) relative to the calculated ground state for each $SrMO_3$. Specifically, the calculated ground states are tetragonal (I4/mcm) for $SrTiO_3$ (panel b in Figure 1), cubic ($Pm\bar{3}m$) for $SrVO_3$, $SrCrO_3$, $SrFeO_3$, and $SrCoO_3$ (panel c), and orthorhombic (C221) for $SrMnO_3$ (panel d), largely consistent with available experimental literature. [33–36]

In the case of $SrMnO_3$, we predict the orthorhombic structure to be more stable than the experimentally observed room temperature hexagonal ($P6_3/mmc$) phase, [37] which can be attributed to possible subtle low-temperature distortions that may be challenging to capture experimentally. In any case, we don't expect the

orthorhombic $SrMnO_3$ phase to be relevant under STWS operating temperatures and utilize the hexagonal structure for subsequent calculations. In terms of the 0 K thermodynamic stability, we find all the calculated ground states of all $SrMO_3$ perovskites considered to be on the convex hull (i.e., E_{hull} =0 meV/atom), except $SrCoO_3$ (E_{hull} ~200 meV/atom) and $SrCrO_3$ (E_{hull} ~30 meV/atom, see Figure S2 of the ESI). The hexagonal-$SrMnO_3$ is above the 0 K Sr-Mn-O convex hull by ~5 meV/atom.

The calculated $E[V_O]$ for the ternary Sr-M-O perovskites are shown in Figure 2 for each M. While the solid bars indicate the lowest (or only) $E[V_O]$ for each system, hollow bars signify the variation in $E[V_O]$ due to differences in the oxygen vacancy configuration within a structure. The dashed blue and red lines indicate the optimal range of $E[V_O]$ used for identifying potential STWS candidates, namely 3.2-4.1 eV, as used in prior literature. [10, 15, 16] We require an optimal $E[V_O]$ since the interactions between the oxide ion and its cation neighbors should be neither too strong (affects thermal reduction) nor too weak (affects spontaneity of water splitting). [15]

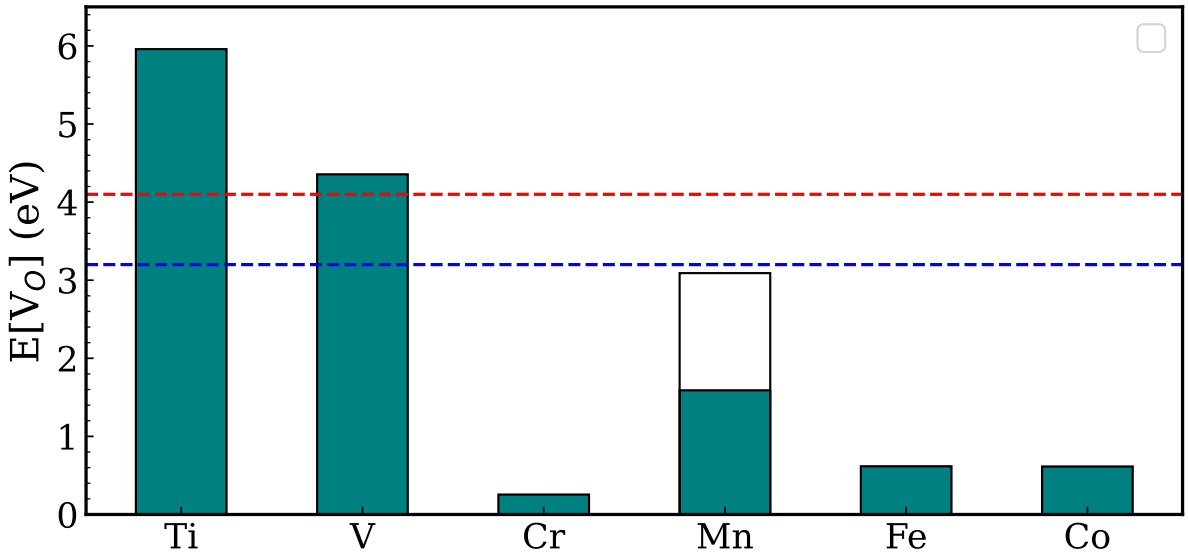

Figure 2: Calculated $E[V_O]$ of the various ground state polymorphs of Sr-M-O ternary perovskites. The blue and red dashed line indicates the optimal range of window of $E[V_O]$ for STWS. For $SrMnO_3$, we considered the experimentally-relevant hexagonal polymorph instead of the ground state orthorhombic structure.

We find the $E[V_O]$ to follow the trends in the crystal reduction potentials of the M^{4+}, suggesting that the ease/difficulty of reducing the transition metal cation plays a crucial role in setting the magnitude of $E[V_O]$ in ternary $SrMO_3$. [32] For example, $SrTiO_3$ exhibits a high $E[V_O]$ (~6 eV, Figure 2), well beyond the optimal 3.2-4.1 eV range, which can be attributed to the low (negative) crystal reduction potential of Ti^{4+}, [32] making it too difficult to reduce under practical STWS conditions. On the other hand, $SrCrO_3$, $SrFeO_3$, and $SrCoO_3$ exhibit low $E[V_O]$ ($\leq$2 eV), indicating insufficient ability to generate H_2. Importantly, we find $SrVO_3$ ($E[V_O]$ ~ 4.35 eV) and hexagonal-$SrMnO_3$ ($E[V_O]$~1.59-3.09 eV) to be promising candidates, with the calculated $E[V_O]$ close to the targeted range. However, the redox-activity of both $SrVO_3$ and $SrMnO_3$ is on the M-site only (see Table S2 of the ESI).

3.2 Quaternary perovskites

To potentially enhance ΔS_{red}, we introduce Ce to the A-site of the $SrMO_3$ ternaries and create $Sr_{0.5}Ce_{0.5}MO_3$ quaternaries. The potential presence of Ce^{4+}, which can reduce to Ce^{3+}, offers the possibility of redox activity at the A site in addition to the B site. Due to the high E[V_O] in ternary-$SrTiO_3$, we did not consider the corresponding quaternary, i.e., $Sr_{0.5}Ce_{0.5}TiO_3$ for further calculations. Upon substitution of Sr with Ce, we used DFT to identify the ground state Sr-Ce configuration within each perovskite, as compiled in Figure 3. Notably, we observe all the quaternary ground state structures to be thermodynamically stable, i.e., E_{hull} =0 meV/atom (Figure S2 of the ESI), indicating their potential synthesizability in experiments.

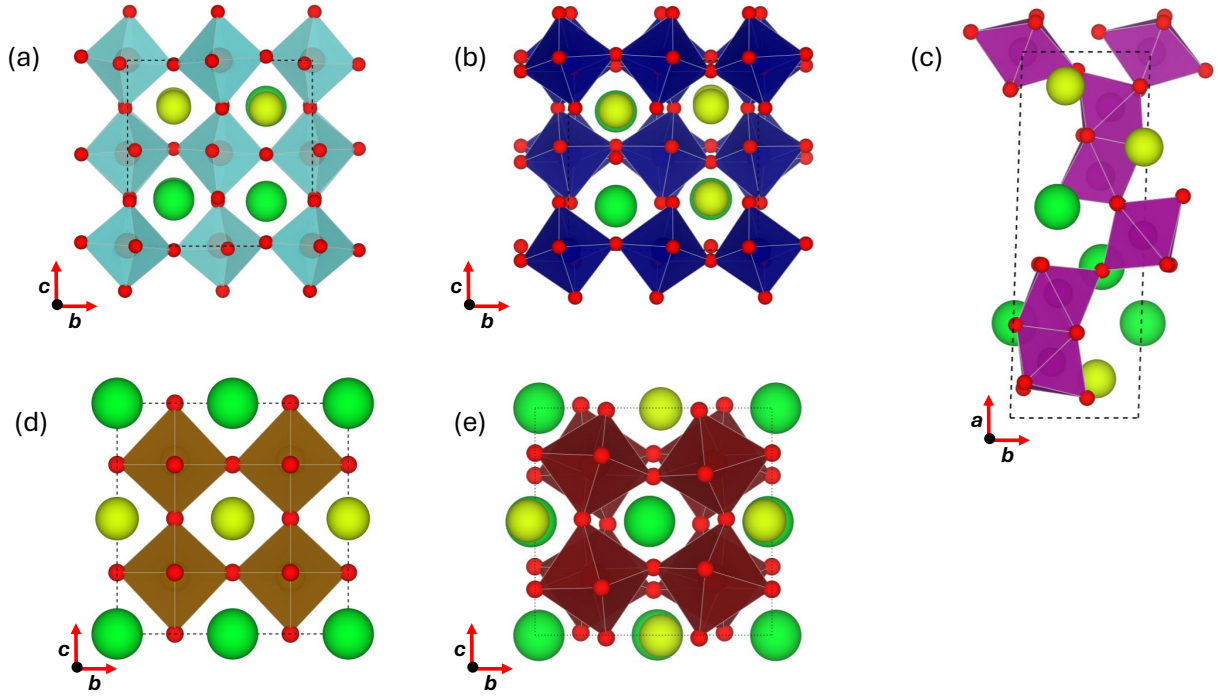

Figure 3: Ground state polymorphs of $Sr_{0.5}Ce_{0.5}MO_3$ based perovskites, with notations similar to Figure 1 and Ce atoms depicted by yellow spheres. (a) $Sr_{0.5}Ce_{0.5}VO_3$, (b) $Sr_{0.5}Ce_{0.5}CrO_3$, (c) $Sr_{0.5}Ce_{0.5}MnO_3$, (d) $Sr_{0.5}Ce_{0.5}FeO_3$, and (e) $Sr_{0.5}Ce_{0.5}CoO_3$.

Figure 4 displays the DFT-calculated E[V_O] for the Sr-Ce-M-O quaternaries considered. The trends in the calculated E[V_O] among the quaternaries do exhibit significant differences compared to the trends in ternary Sr-M-O, which can be due to the electrostatic and possible redox contributions of Ce. For example, the calculated E[V_O] do not differ by ~4 eV between the Sr-Ce-V-O and Sr-Ce-Cr-O quaternaries, unlike the Sr-V-O and Sr-Cr-O ternaries.

Notably, $Sr_{0.5}Ce_{0.5}VO_3$ shows E[V_O] between 5.28−5.54 eV, which is too high for efficient STWS, despite the potential for V-site redox in ternary Sr-V-O. Also, $Sr_{0.5}Ce_{0.5}FeO_3$ and $Sr_{0.5}Ce_{0.5}CoO_3$ exhibit low E[V_O] ($\leq$2.2 eV), making them unsuitable, similar to their ternary counterparts. Importantly, we find $Sr_{0.5}Ce_{0.5}MnO_3$ and $Sr_{0.5}Ce_{0.5}CrO_3$ to be promising candidates for SWTS, given their calculated E[V_O], namely 2.81-3.87 eV and 4.03-4.83 eV, overlap with our target range of 3.2-4.1 eV. Note that Mn is a recurring redox-active element of importance among perovskites for STWS, since Mn-containing compositions have been demonstrated before as promising STWS candidates. [15, 16, 38]

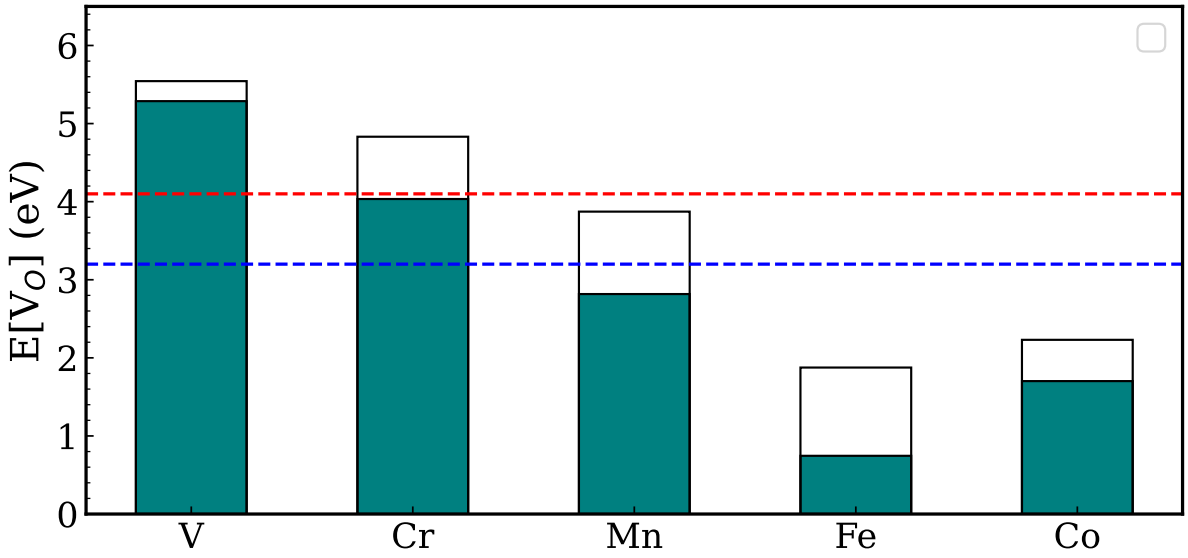

Figure 4: Oxygen vacancy formation energies of the various ground state polymorphs of Sr and Ce based quarternary perovskites. The blue and red dashed line indicates the suitable window of oxygen vacancy formation energies for STC application. $Sr_{0.5}Ce_{0.5}CrO_3$ and $Sr_{0.5}Ce_{0.5}MnO_3$ have values closer to the optimal range and are suitable candidates.

Although we do not observe any dual cation redox at 0 K in any of the Sr-Ce-M-O quaternaries (see Table S3 of the ESI), as indicated by changes in on-site magnetic moments, we expect multiple redox mechanisms to be activated at higher temperatures as vacancy concentration increases and higher energy vacancy configurations form. Simultaneous redox activity can also be induced by doping elements in addition to Ce on the B-site and/or on the A-site to form quinary and higher component Sr-perovskites.

4 Conclusion

In conclusion, we systematically investigated ternary $SrMO_3$ and quaternary $Sr_{0.5}Ce_{0.5}MO_3$ (M = Ti, V, Cr, Mn, Fe, or Co) perovskites for STWS using DFT-based calculations. We identified the ground state structures of both ternaries and quaternaries, evaluated their 0 K thermodynamic stability and calculated E[V_O]. Importantly, we found $SrMnO_3$ and $SrVO_3$ among ternaries, and $Sr_{0.5}Ce_{0.5}MnO_3$ and $Sr_{0.5}Ce_{0.5}CrO_3$ among quaternaries to be promising candidates, as indicated by the overlap of calculated E[V_O] with the optimal range of 3.2-4.1 eV. Our findings highlight a promising chemical strategy for designing advaned STWS materials that enable efficient green H_2 generation and will be useful in the exploration of other higher-component oxide perovskites for STWS and beyond.

Conflicts of interest

The authors declare no conflicts of interest.

Acknowledgements

G.S.G. acknowledges financial support from Tata Consultancy Services (TCS). The authors acknowledge the computational resources provided by the Supercomputer Education and Research Centre (SERC), IISc and useful discussions with Dr. Sriram Goverapet Srinivasan of TCS.

Data availability

The data that support the findings of this study are available from the corresponding author upon reasonable request.

References

[1] International Energy Agency. World energy outlook 2023. Technical report, IEA, Paris, 2023.

[2] Nicola Armaroli and Vincenzo Balzani. The future of energy supply: challenges and opportunities. *Angew. Chem. Int. Ed.*, 46:52–66, 2007.

[3] John A. Turner. A realizable renewable energy future. *Science*, 285(5428):687–689, 1999.

[4] P. M. Falcone, M. Hiete, and A. Sapio. Hydrogen economy and sustainable development goals: review and policy insights. *Curr. Opin. Green Sustain. Chem.*, 31:100506, 2021.

[5] Aldo Steinfeld. Solar thermochemical production of hydrogen—a review. *Solar Energy*, 78(5):603–615, 2005.

[6] Christos Agrafiotis, Martin Roeb, and Christian Sattler. A review on solar thermal syngas production via redox pair-based water/carbon dioxide splitting thermochemical cycles. *Renew. Sustain. Energy Rev.*, 42:254–285, 2015.

[7] William C. Chueh and Sossina M. Haile. Ceria as a thermochemical reaction medium for selectively generating syngas or methane from H_2O and CO_2. *ChemSusChem*, 2(8):735–739, 2009.

[8] Christopher Muhich and Aldo Steinfeld. Principles of doping ceria for the solar thermochemical redox splitting of h 2 o and co 2. *J. Mater. Chem. A*, 5(30):15578–15590, 2017.

[9] Michael Bulfin, Johannes Vieten, Felix Call, Martin Lange, August Francke, Martin Roeb, and Christian Sattler. Thermodynamics of ceria reduction and oxidation for solar thermochemical applications. *J. Mater. Chem. A*, 5:1152–1160, 2017.

[10] Robert B Wexler, Ellen B Stechel, and Emily A Carter. Materials design directions for solar thermochemical water splitting. *Solar Fuels*, pages 1–63, 2023.

[11] Anthony H. McDaniel, Elizabeth C. Miller, Dodi Arifin, Andrea Ambrosini, Eric N. Coker, Ryan O'Hayre, William C. Chueh, and Jijie Tong. Sr− and mn−doped laalo$_{3-\delta}$ for solar thermochemical h$_2$ and co production. *Energy Environ. Sci.*, 6:2424–2428, 2013.

[12] Johannes Vieten, Brendan Bulfin, Felix Call, Martin Lange, Marcus Schmücker, August Francke, Martin Roeb, and Christian Sattler. Perovskite oxides for application in thermochemical air separation and oxygen storage. *J. Mater. Chem. A*, 4(35):13652–13659, 2016.

[13] Matthew D Witman, Anuj Goyal, Tadashi Ogitsu, Anthony H McDaniel, and Stephan Lany. Defect graph neural networks for materials discovery in high-temperature clean-energy applications. *Nat. Comp. Sci.*, 3(8):675–686, 2023.

[14] S Shahab Naghavi, Antoine A Emery, Heine A Hansen, Fei Zhou, Vidvuds Ozolins, and Chris Wolverton. Giant onsite electronic entropy enhances the performance of ceria for water splitting. *Nat. Comm.*, 8(1):285, 2017.

[15] Gopalakrishnan Sai Gautam, Ellen B. Stechel, and Emily A. Carter. Exploring ca–ce–m–o (m=3d transition metal) oxide perovskites for solar thermochemical applications. *Chem. Mater.*, 32(23):9964–9982, 2020.

[16] Robert B Wexler, Gopalakrishnan Sai Gautam, Robert T Bell, Sarah Shulda, Nicholas A Strange, Jamie A Trindell, Joshua D Sugar, Eli Nygren, Sami Sainio, Anthony H McDaniel, et al. Multiple and nonlocal cation redox in ca–ce–ti–mn oxide perovskites for solar thermochemical applications. *Energy Environ. Sci.*, 16(6):2550–2560, 2023.

[17] Ke Gao, Xianglei Liu, Qi Wang, Zhixing Jiang, Cheng Tian, Nan Sun, and Yimin Xuan. Remarkable solar thermochemical co 2 splitting performances based on ce-and al-doped srmno 3 perovskites. *Sustain. Energy Fuels*, 7(4):1027–1040, 2023.

[18] Su Jeong Heo, Michael Sanders, Ryan O'Hayre, and Andriy Zakutayev. Double-site substitution of ce into (ba, sr) mno3 perovskites for solar thermochemical hydrogen production. *ACS Energy Lett.*, 6(9):3037–3043, 2021.

[19] Emily Krzystowczyk, Xijun Wang, Jian Dou, Vasudev Haribal, and Fanxing Li. Substituted srfeo 3 as robust oxygen sorbents for thermochemical air separation: correlating redox performance with compositional and structural properties. *Phys. Chem. Chem. Phys.*, 22(16):8924–8932, 2020.

[20] Y Takeda, T Hashino, H Miyamoto, F Kanamaru, S Kume, and M Koizumi. Synthesis of srnio3 and related compound, sr2ni2o5. *J. Inorg. Nucl. Chem.*, 34(5):1599–1601, 1972.

[21] Gopalakrishnan Sai Gautam, Ellen B Stechel, and Emily A Carter. A first-principles-based sub-lattice formalism for predicting off-stoichiometry in materials for solar thermochemical applications: The example of ceria. *Adv. Theory Simul.*, 3(9):2000112, 2020.

[22] Georg Kresse and Jürgen Furthmüller. Efficient iterative schemes for *ab initio* total-energy calculations using a plane-wave basis set. *Phys. Rev. B*, 54(16):11169–11186, 1996.

[23] Georg Kresse and J. Hafner. *Ab initio* molecular dynamics for liquid metals. *Phys. Rev. B*, 47(1):558–561, 1993.

[24] Georg Kresse and David Joubert. From ultrasoft pseudopotentials to the projector augmented-wave method. *Phys. Rev. B*, 59(3):1758–1775, 1999.

[25] Jianwei Sun, Adrienn Ruzsinszky, and John P. Perdew. Strongly constrained and appropriately normed semilocal density functional. *Phys. Rev. Lett.*, 115:036402, 2015.

[26] Gopalakrishnan Sai Gautam and Emily A Carter. Evaluating transition metal oxides within dft-scan and scan+ u frameworks for solar thermochemical applications. *Phys. Rev. Mater.*, 2(9):095401, 2018.

[27] Olivia Y Long, Gopalakrishnan Sai Gautam, and Emily A Carter. Evaluating optimal u for 3 d transition-metal oxides within the scan+ u framework. *Phys. Rev. Mater.*, 4(4):045401, 2020.

[28] S Swathilakshmi, Reshma Devi, and Gopalakrishnan Sai Gautam. Performance of the r2scan functional in transition metal oxides. *J. Chem. Theory Comput.*, 19(13):4202–4215, 2023.

[29] Hendrik J Monkhorst and James D Pack. Special points for brillouin-zone integrations. *Phys. Rev. B*, 13(12):5188, 1976.

[30] Michael Hellenbrandt. The inorganic crystal structure database (icsd)—present and future. *Crystallogr. Rev.*, 10(1):17–22, 2004.

[31] Shyue Ping Ong, William D. Richards, Anubhav Jain, Geoffroy Hautier, Minseok Kocher, Shreyas Cholia, Daniel Gunter, Vincent L. Chevrier, Kristin A. Persson, and Gerbrand Ceder. Python materials genomics (pymatgen): a robust, open-source python library for materials analysis. *Comput. Mater. Sci.*, 68:314–319, 2013.

[32] Robert B. Wexler, Gopalakrishnan Sai Gautam, Ellen B. Stechel, and Emily A. Carter. Factors Governing Oxygen Vacancy Formation in Oxide Perovskites. *J. Am. Chem. Soc.*, 143(33):13212–13227, August 2021. Publisher: American Chemical Society.

[33] Y. C. Lan, X. L. Chen, and M. He. Structure, magnetic susceptibility and resistivity properties of $SrVO_3$. *J. Alloys Compd.*, 354:95–98, 2003.

[34] Zhong-Li Zhu, Jian-Hong Gu, Yu Jia, and Xian Hu. A comparative study of electronic structure and magnetic properties of $SrCrO_3$ and $SrMoO_3$. *Physica B Condens. Matter*, 407:1990–1994, 2012.

[35] Yong Wang, Jian Chen, and Xueyi Wu. Preparation and gas-sensing properties of perovskite-type $SrFeO_3$ oxide. *Mater. Lett.*, 49(6):361–364, 2001.

[36] Pavel Bezdicka, Alain Wattiaux, Jean-Claude Grenier, Michel Pouchard, and Paul Hagenmuller. Preparation and characterization of fully stoichiometric $SrCoO_3$ by electrochemical oxidation. *Z. Anorg. Allg. Chem.*, 619(1):7–12, 1993.

[37] Fuxiao Dong, Gefei Lu, Qinghua Ma, Bojun Zhao, Haiou Wang, Dexuan Huo, and Weishi Tan. Structure and magnetic properties of the manganite srmno3. *J. Mater. Sci.: Mater. Electron.*, 34(36):2322, 2023.

[38] Debora R. Barcellos, Michael D. Sanders, Jianhua Tong, Anthony H. McDaniel, and Ryan P. O'Hayre. $Bace_{0.25}mn_{0.75}o_{3-\delta}-$ a promising perovskite-type oxide for solar thermochemical hydrogen production. *Energy Environ. Sci.*, 11:3256–3265, 2018.

5 Electronic supplementary information

SI. Overall solar thermochemical reaction

The single-step thermal dissociation of H_2O:

$$H_2O \rightleftharpoons H_2 + \frac{1}{2}\,O_2 \tag{S1}$$

The two-step solar thermochemical water splitting (STWS) cycle for a perovskite AMO_3, where M is a redox-active transition metal and A is a 'large' cation:

$$AMO_3 \longrightarrow AMO_{3-\delta} + \frac{\delta}{2}\,O_2 \quad \text{(Thermal Reduction, TR)} \tag{S2}$$

$$AMO_{3-\delta} + \delta H_2O \longrightarrow AMO_3 + \delta H_2 \quad \text{(Water Splitting, WS)} \tag{S3}$$

The overall reaction by summing (S2) and (S3):

$$\delta H_2O \longrightarrow \delta H_2 + \frac{\delta}{2}\,O_2 \tag{S4}$$

SII. Crystal Structures

Table S1 lists the ternary $SrMO_3$ polymorphs considered in this study, along with their space groups and collection codes from the inorganic crystal structure database (ICSD), where M = Ti, V, Cr, Mn, Fe, or Co. We used the listed structures as initial guesses for density functional theory (DFT) based calculations to identify the ground state polymorph of each $SrMO_3$ composition.

Table S1: ICSD collection codes and space groups for ternary $SrMO_3$ polymorphs.

System	Space Group	ICSD Collection Code
$SrTiO_3$	I4/mcm	182762
	$Pm\bar{3}m$	80873
$SrVO_3$	$Pm\bar{3}m$	88982
$SrCrO_3$	$Pm\bar{3}m$	108903
$SrMnO_3$	C221	157936
	$P6_3/mmc$	185417
	$Pm\bar{3}m$	17243
	$P6_3$	17245
$SrFeO_3$	$Pm\bar{3}m$	92335
$SrCoO_3$	$Pm\bar{3}m$	77142
	$P12_1/m1$	108896

SIII. Convex hulls

We evaluated the thermodynamic stability of the ternary $SrMO_3$ and quaternary $Sr_{0.5}Ce_{0.5}MO_3$ perovskites by constructing the 0 K convex hull based on DFT-calculated total energies. Figure S1 shows the ternary convex hulls for the Sr-M-O systems, while Figure S2 shows relevant ternary projections of the quaternary convex hulls for the Sr-Ce-M-O systems. Perovskite compositions that lie on the hull (green dots) are predicted to be thermodynamically stable with respect to decomposition into other competing phases (black dots). Red dots indicate metastable/unstable perovskite compositions.

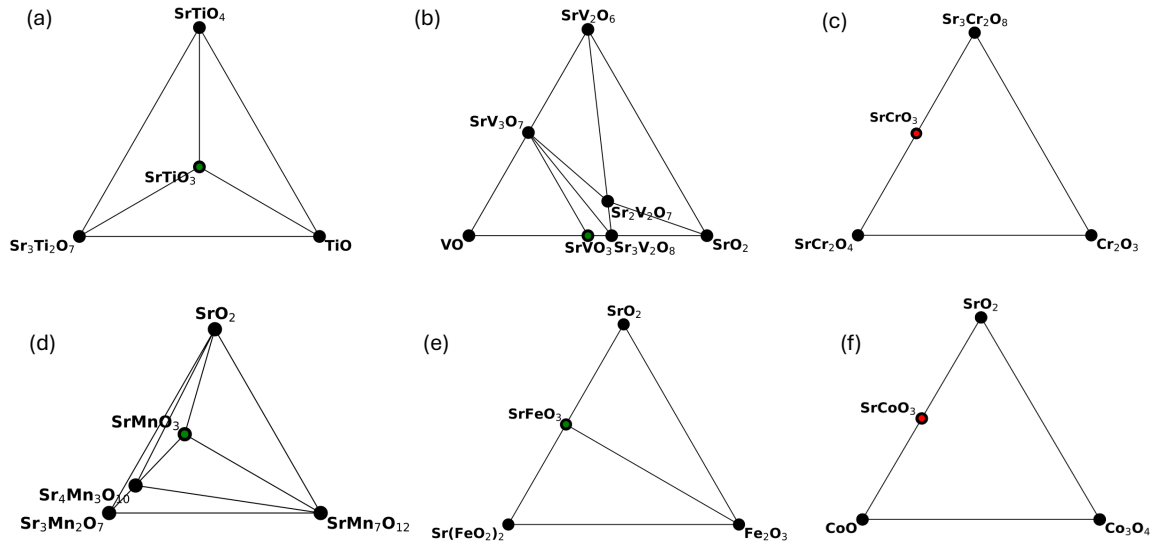

Figure S1: Calculated 0 K convex hulls of ternary Sr-M-O systems, namely, (a) Sr-Ti-O, (b) Sr-V-O, (c) Sr-Cr-O, (d) Sr-Mn-O, (e) Sr-Fe-O, and (f) Sr-Co-O. Green (red) dots indicate that the perovskite compositions of interest lies on (above) the hull, with respect to the other competing phases (black dots). The thermodynamic decomposition products of $SrCoO_3$ are SrO_2, $Sr_2Co_2O_5$ and $SrCo_6O_{11}$, while that of $SrCrO_3$ are $SrCr_2O_4$ and $Sr_3Cr_2O_8$

.

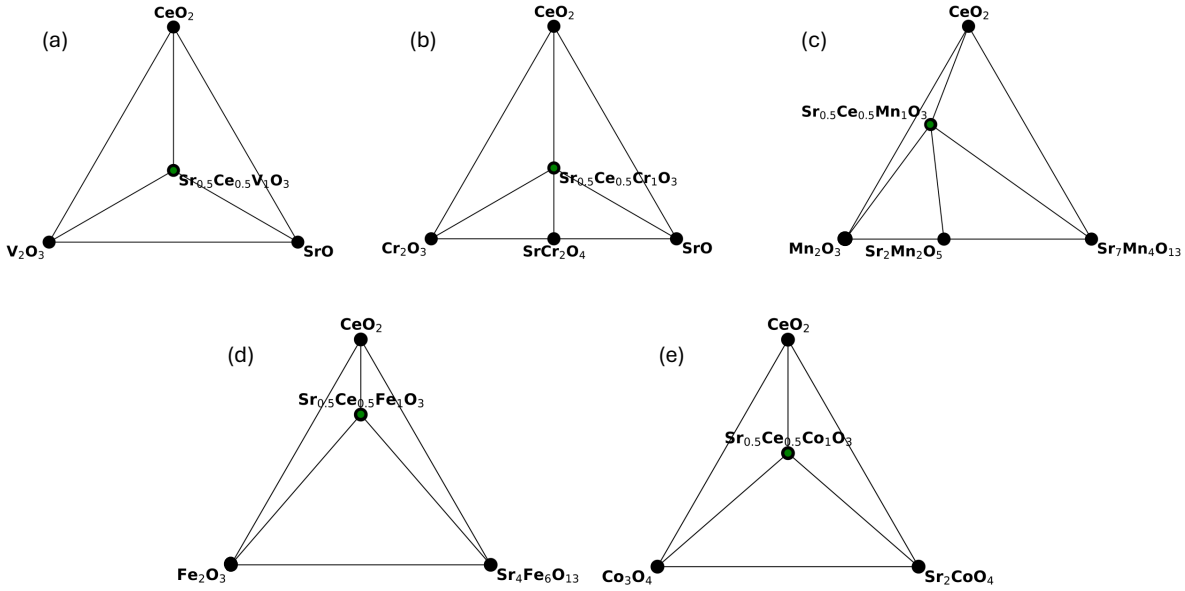

Figure S2: Calculated 0 K convex hulls of quaternary Sr-Ce-M-O systems, namely, (a) Sr-Ce-V-O, (b) Sr-Ce-Cr-O, (c) Sr-Ce-Mn-O, (d) Sr-Ce-Fe-O, and (e) Sr-Ce-Co-O. Since quaternary convex hulls are 3D entities, we display relevant 2D projections containing the $Sr_{0.5}Ce_{0.5}MO_3$ perovskites of interest for ease of visualization. Notations used are similar to Figure S1.

SIV. Oxidation states

Table S2: Oxidation states of Sr and M cations in Sr-M-O ternaries in pristine and defect structures, based on calculated on-site magnetic moments. V exhibits mixed oxidation states in the pristine as well as defective $SrVO_3$ structure. Fe does not exhibit a noticeable change in its magnetic moment upon defect formation in $SrFeO_3$. Co exhibits both low-spin and high-spin configurations on its Co^{4+} and Co^{3+} sites upon defect formation in $SrCoO_3$.

M-site	Compound	Sr oxidation state	M oxidation state
Ti	Pristine	Sr^{2+}	Ti^{4+}
	Defect	Sr^{2+}	$Ti^{4+/3+}$
V	Pristine	Sr^{2+}	$V^{4+/3+}$
	Defect	Sr^{2+}	$V^{4+/3+}$
Cr	Pristine	Sr^{2+}	Cr^{4+}
	Defect	Sr^{2+}	$Cr^{4+/3+}$
Mn	Pristine	Sr^{2+}	Mn^{4+}
	Defect	Sr^{2+}	$Mn^{4+/3+}$
Fe	Pristine	Sr^{2+}	Fe^{4+}
	Defect	Sr^{2+}	Fe^{4+}
Co	Pristine	Sr^{2+}	Co^{4+}
	Defect	Sr^{2+}	$Co^{4+/3+}$

Table S3: Oxidation states of Ce and M cations in $Sr_{0.5}Ce_{0.5}MO_3$ perovskites in pristine and defect structures, based on calculated on-site magnetic moments. Sr exhibits the 2+ oxidation state in both the defective and pristine structures of all quaternaries considered. Although the Cr and Co systems contain Ce in its 4+ oxidation state, with potential for reduction to Ce^{3+}, we do not observe any noticeable change in the on-site magnetic moments of Ce^{4+} upon defect formation in the quaternary structures, citing the sole participation of the transitiuon metal in the reduction. The Fe-containing quaternary exhibited an extent of disproportionation upon defect formation, i.e., Ce^{3+} oxidized in addition to Fe^{4+} reduction upon defect formation.

M-site	Compound	Ce oxidation state	M oxidation state
V	Pristine	Ce^{3+}	$V^{4+/3+}$
	Defect	Ce^{3+}	$V^{4+/3+}$
Cr	Pristine	Ce^{4+}	Cr^{3+}
	Defect	Ce^{4+}	$Cr^{3+/2+}$
Mn	Pristine	Ce^{3+}	$Mn^{4+/3+}$
	Defect	Ce^{3+}	$Mn^{4+/3+}$
Fe	Pristine	Ce^{3+}	$Fe^{4+/3+}$
	Defect	Ce^{4+}	$Fe^{4+/3+}$
Co	Pristine	Ce^{4+}	Co^{3+}
	Defect	Ce^{4+}	$Co^{3+/2+}$

SV. Convex hull calculations

ICSD collection codes of all ordered unary, binary, ternary, and quaternary Sr-Ce-M-O structures considered are compiled below, as grouped by M (transition metal, M = Ti, V, Cr, Mn, Fe, Co, or Ni), Ce, and Sr. Note that we did not consider intermetallic phases (e.g., Sr-M, Ce-M, M-M', Sr-Ce-M, etc.) in our convex hull calculations.

Titanium-containing compounds (Ti)

Compound	ICSD ID	Compound	ICSD ID
Ti	43416	TiO	15327
TiO_2	9191	Ti_2O	23574
Ti_2O_3	6095	Ti_3O	20041
Ti_3O_5	75194	Ti_4O_5	77697
Ti_4O_7	6098	Ti_5O_9	9038
Ti_6O	17009	Ti_6O_{11}	35121
Ti_7O_{13}	35122	Ti_8O_{15}	35123
Ti_9O_{17}	35124	$SrTi_{11}O_{20}$	71299
$Sr_2Ti_6O_{13}$	10455	$Sr_3Ti_2O_7$	63704
$SrTiO_3$	182762	$SrTiO_4$	194713

Vanadium-containing compounds (V)

Compound	ICSD ID	Compound	ICSD ID
V	43420	VO	28681
VO_2	15889	V_2O_3	6286
V_2O_5	24042	V_3O_5	16445
V_3O_7	2338	V_4O_7	2775
V_4O_9	15041	V_5O_9	6097
V_6O_{11}	196	V_6O_{13}	15028
V_7O_3	77706	V_7O_{13}	197
V_8O	166600	V_8O_{15}	424885
V_9O_{17}	424886	$V_{13}O_{16}$	77708
$V_{16}O_3$	77707	SrV_3O_7	72604
SrV_6O_{15}	98574	SrV_2O_6	65928
$Sr_2V_2O_7$	10330	$Sr_4V_3O_{10}$	73698
Sr_2VO_4	69000	SrV_6O_{11}	71868
$Sr_3V_2O_8$	54655	SrV_4O_9	90926
$SrV_{13}O_{18}$	97949	$Sr_3V_2O_7$	71320
$SrV_{10}O_{15}$	15273		

Chromium-containing compounds (Cr)

Compound	ICSD ID	Compound	ICSD ID
Cr	44731	CrO	109296
CrO_2	9423	CrO_3	16031
Cr_2O_3	25781	Cr_3O	15904
Cr_5O_{12}	24299	Cr_8O_{21}	71297
$Sr_9Cr_5O_{18}$	91252	$SrCr_2O_4$	6132
$SrCr_{10}O_{15}$	85053	Sr_2CrO_4	26944
$Sr_4Cr_3O_9$	85045	$SrCrO_3$	245834
$SrCrO_4$	259674	$SrCrO_4$	259675
$Sr_4Cr_3O_{10}$	257906	$Sr_3Cr_2O_8$	85055
$SrCr_2O_7$	28411		

Manganese-containing compounds (Mn)

Compound	ICSD ID	Compound	ICSD ID
Mn	5248	MnO	9864
MnO_2	393	Mn_2O_3	24342
Mn_2O_7	60821	Mn_3O_4	8355
Mn_5O_8	16956	$Sr_7Mn_4O_{15}$	72332
$Sr_3Mn_2O_7$	51215	$Sr_5Mn_5O_{13}$	159660
$Sr_2Mn_2O_5$	90184	$Sr_2Mn_2O_5$	90183
Sr_2MnO_4	26560	$Sr_7Mn_4O_{13}$	160291
$SrMnO_3$	17243	$SrMn_7O_{12}$	195757
$Sr_4Mn_3O_{10}$	81351		

Iron-containing compounds (Fe)

Compound	ICSD ID	Compound	ICSD ID
Fe	14754	FeO	31081
Fe_2O_3	7797	Fe_3O_4	5247
Fe_4O_5	434152	Fe_5O_7	430563
Fe_7O_9	430601	Fe_7O_{10}	135154
$Fe_{13}O_{19}$	238770	$Fe_{25}O_{32}$	430562
$SrFeO_2$	173434	$SrFeO_3$	58460
Sr_2FeO_3	251018	Sr_2FeO_4	74419
$Sr(FeO_2)_2$	94350	$Sr_3(FeO_3)_2$	74434
$Sr_2Fe_2O_5$	51318	$Sr_2Fe_2O_5$	247823
$Sr_3Fe_2O_5$	261512	$Sr_3Fe_2O_7$	2648
$Sr_4Fe_4O_{11}$	91064	$Sr_4Fe_6O_{12}$	290200
$Sr_4Fe_6O_{13}$	63621	$Sr_8Fe_8O_{23}$	91063
$Sr_{25}Fe_{30}O_{77}$	118097	$Sr_2(FeO_2)_3$	290200

Cobalt-containing compounds (Co)

Compound	ICSD ID	Compound	ICSD ID
Co	36675	CoO	9865
CoO_2	88722	Co_3O_4	24210
$Sr_2Co_2O_5$	162239	$Sr_2Co_2O_5$	162240
$Sr_2Co_2O_5$	173696	$Sr_8Co_8O_{23}$	245305
$Sr_6(CoO_3)_5$	173698	$Sr_6(CoO_3)_5$	81312
SrCoO	155223	$SrCoO_3$	108896
Sr_2CoO_3	99894	$Sr_5(CoO_3)_4$	88628
$Sr_3(CoO_3)_2$	182288	$SrCo_6O_{11}$	152279
Sr_2CoO_4	246483		

Cerium-containing compounds (Ce)

Compound	ICSD ID	Compound	ICSD ID
Ce	41823	CeO	52886
CeO_2	70257	Ce_2O_3	621706
Ce_7O_{12}	88754	$SrCeO_3$	71352
$CeVO_3$	99835	$CeCrO_3$	28931
$CeMn_7O_{12}$	8773	$CeCrO_3$	28931
$CeVO_3$	99835		

Strontium-containing compounds (Sr)

Compound	ICSD ID	Compound	ICSD ID
Sr	44721	SrO	19987
SrO_2	24249		